RESEARCH ARTICLE | FEBRUARY 20 2025

Polariton spectra under the collective coupling regime. II. 2D non-linear spectra

Special Collection: David Jonas Festschrift

M. Elious Mondal ; A. Nickolas Vamivakas ; Steven T. Cundiff ; Todd D. Krauss ; Pengfei Huo

J. Chem. Phys. 162, 074110 (2025)
https://doi.org/10.1063/5.0249705
CHORUS

The Journal of Chemical Physics ARTICLE pubs.aip.org/aip/jcp

Polariton spectra under the collective coupling regime. II. 2D non-linear spectra

Cite as: J. Chem. Phys. 162, 074110 (2025); doi: 10.1063/5.0249705
Submitted: 19 November 2024 • Accepted: 30 January 2025 •
Published Online: 20 February 2025

M. Elious Mondal,[1,a)] A. Nickolas Vamivakas,[2,3,4] Steven T. Cundiff,[5] Todd D. Krauss,[1,2,3] and Pengfei Huo[1,2,3,b)]

AFFILIATIONS

[1] Department of Chemistry, University of Rochester, Rochester, New York 14627, USA
[2] The Institute of Optics, Hajim School of Engineering, University of Rochester, Rochester, New York 14627, USA
[3] Center for Coherence and Quantum Optics, University of Rochester, Rochester, New York 14627, USA
[4] Department of Physics and Astronomy, University of Rochester, Rochester, New York 14627, USA
[5] Department of Physics, University of Michigan, Ann Arbor, Michigan 48109, USA

Note: This paper is part of the JCP Special Topic, David Jonas Festschrift.
[a)] **Electronic mail:** mmondal@ur.rochester.edu
[b)] **Author to whom correspondence should be addressed:** pengfei.huo@rochester.edu

ABSTRACT

In our previous work [Mondal *et al.*, J. Chem. Phys. **162**, 014114 (2025)], we developed several efficient computational approaches to simulate exciton–polariton dynamics described by the Holstein–Tavis–Cummings (HTC) Hamiltonian under the collective coupling regime. Here, we incorporated these strategies into the previously developed Lindblad-partially linearized density matrix ($\mathcal{L}$-PLDM) approach for simulating 2D electronic spectroscopy (2DES) of exciton–polariton under the collective coupling regime. In particular, we apply the efficient quantum dynamics propagation scheme developed in Paper I to both the forward and the backward propagations in the PLDM and develop an efficient importance sampling scheme and graphics processing unit vectorization scheme that allow us to reduce the computational costs from $\mathcal{O}(\mathcal{K}^2)\mathcal{O}(T^3)$ to $\mathcal{O}(\mathcal{K})\mathcal{O}(T^0)$ for the 2DES simulation, where $\mathcal{K}$ is the number of states and T is the number of time steps of propagation. We further simulated the 2DES for an HTC Hamiltonian under the collective coupling regime and analyzed the signal from both rephasing and non-rephasing contributions of the ground state bleaching, excited state emission, and stimulated emission pathways.

I. INTRODUCTION

Nonlinear spectroscopy can be a very powerful measurement tool that provides a fundamental understanding of the photophysics of polariton systems by unraveling the energy transfer mechanisms through lineshape features and lifetimes of the different peak intensities.[1–8] Transient absorption (TA) measurements by DelPo *et al.*[9] studies non-linear effects such as excited state absorption (ESA) to doubly excited polariton states. Virgili *et al.*[10] have developed kinetic models suggesting indirect energy transfer from upper polariton (UP) to lower polariton (LP) via dark states. Although TA is a powerful tool to investigate polariton photophysics, one should be cautious about the potential optical artifacts, as pointed out in Refs. 11 and 12. On the other hand, 2D electronic spectroscopy, as pioneered by Jonas[13–16] and many others,[17–22] can easily overcome these challenges by resolving the system dynamics along two frequency axes.[19–21,23–27] The various non-linear effects that result from collective coupling in exciton–polariton systems such as derivative lineshapes from ESA transitions,[9] motional narrowing,[28–30] polaron decoupling,[1,6,7] and coherence enhancement[6,7,31] can be directly studied by just studying the 2D lineshapes of the diagonal and cross peaks and how these signals evolve in time. Takahashi and Watanabe[1] demonstrated the effect of polaron decoupling in exciton–polaritons using tetraphenyldibenzoperiflanthene (DBP) molecules coupled to a cavity, appearing as a tilt of the slope between the GSB (ground state bleach) + SE (stimulated emission) and ESA (excited state absorption) signals in the lower polariton peak. A similar study has been done by Quenzel and co-workers,[6,7] where

they couple Squarine J-aggregates to gold plasmonic surfaces and observe the slope tilt in the polariton 2DES peaks. Recent 2DES measurements also demonstrate energy relaxation and energy transfer mechanisms in different types of exciton–polariton systems, including J-aggregates[5–7] and carbon nanotubes.[3] These studies[3,7] also demonstrate the enhancement of exciton lifetimes and coherent energy transfer lifetimes[32,33] due to the collective coupling of molecules to the cavity mode.

Despite the rich amount of information that can be extracted by the 2DES signals, there is only a limited amount of theoretical work on simulating 2DES for exciton polariton.[8,34–36] In our previous work,[8] we developed a theoretical approach for simulating linear and non-linear spectroscopy of exciton–polaritons within the semi-classical partially linearized path-integral framework, but it was limited to $N = 1$ molecule. This is because, with an increasing number of molecules N, the number of states within the second excitation manifold expands quadratically in order of $\mathcal{O}(N^2)$ and the Hamiltonian size scales as $\mathcal{O}(N^4)$. Due to this quartic scaling, the direct computation of dynamical properties for an N-molecule polaritonic system becomes very expensive even for a system as small as $N = 10$.

To efficiently simulate the collective coupling in exciton–polaritons, we have developed efficient quantum dynamics propagation schemes, reported in Paper I.[37] In particular, we take advantage of the sparsity of the HTC Hamiltonian and develop an efficient propagation scheme based on the Chebyshev series expansion of the time evolution operator. In this paper, we integrate our theoretical development in Ref. 8 and in Paper I[37] to simulate 2DES of N-molecules polariton systems, while introducing new algorithms for the focusing step in $\mathcal{L}$-PLDM 2DES calculations. These new developments reduce the cost of the calculations to the order $\mathcal{O}(N^2)$ without the necessity for generating any $\mathcal{O}(N^4)$ matrix. We further show that our algorithm can be efficiently vectorized using graphics processing unit (GPU) to reduce the scaling of 2DES propagation time from $\mathcal{O}(T^3)$ to $\mathcal{O}(T^0)$, where T is the number of propagation steps for each laser in the simulation. This allows us to efficiently perform accurate 2DES calculations, with the help of GPU, for polariton systems with $N \approx \mathcal{O}(10^2)$ where the total states can be of order $\mathcal{O}(10^4)$. We demonstrate the 2DES for up to $N = 25$ molecules coupled to the cavity at $t_2 = 0$ fs and also demonstrate the signal breakdown of 2DES for $N = 5$ molecule polariton system at different population time t_2. Finally, we analyzed the features of different signals from both rephasing and non-rephasing contributions while also further decomposing them as ground-state bleaching (GSB), excited state emission (ESA), and stimulated emission (SE) pathways.

II. THEORETICAL APPROACH

A. Model Hamiltonian

We describe the system of N-molecules coupled to a single cavity mode by the Holstein–Tavis–Cummings (HTC)[38] Hamiltonian,

$$\hat{H} = \hat{H}_{\mathrm{Q}} + \hat{H}_{\mathrm{b}}, \tag{1}$$

where $\hat{H}_{\mathrm{Q}}$ is the quantum part of the Hamiltonian and $\hat{H}_{\mathrm{b}}$ is the phonon bath degrees of freedom (DOF). In particular, we have N excitonic DOF and one photonic mode in $\hat{H}_{\mathrm{Q}}$, together with the exciton–photon interaction as well as the exciton–phonon interactions,

$$\hat{H}_{\mathrm{Q}} = \sum_{n}^{N} \varepsilon_n \hat{\sigma}_n^{\dagger}\hat{\sigma}_n + \hbar\omega_{\mathrm{c}}\left(\hat{a}^{\dagger}\hat{a} + \frac{1}{2}\right) + \sum_{n} \hbar g_{\mathrm{c}}^{n}\left(\hat{\sigma}_n^{\dagger}\hat{a} + \hat{\sigma}_n\hat{a}^{\dagger}\right) + \hat{H}_{\mathrm{sb}}, \tag{2}$$

where the nth exciton has site energy of ε_n and the exciton is coupled to the cavity mode of energy $\hbar\omega_{\mathrm{c}}$ with a light–matter coupling strength of $\hbar g_{\mathrm{c}}^{n}$. Here, $\hat{\sigma}_n^{\dagger} = |e_n\rangle\langle g_n|$ and $\hat{\sigma}_n = |g_n\rangle\langle e_n|$ creates and annilates an excitation on the nth molecule, respectively, with $|g_n\rangle$ and $|e_n\rangle$ as the ground and excited states for molecule n. In addition, each exciton site is also coupled to a set of harmonic bath coordinates ν, which are described by the bath Hamiltonian,

$$\hat{H}_{\mathrm{b}} = \frac{1}{2}\sum_{n=1}^{N}\sum_{\nu}\left(\hat{P}_{n,\nu}^2 + \omega_{n,\nu}^2\hat{R}_{n,\nu}^2\right), \tag{3}$$

where $\hat{P}_{n,\nu}$ and $\hat{R}_{n,\nu}$ are the momentum and position operator, respectively, of the νth phonon on nth exciton. For the HTC Hamiltonian [Eq. (1)], the bath coordinates are diagonally coupled to the exciton, with a bi-linear system–bath interaction defined as

$$\hat{H}_{\mathrm{sb}} = \sum_{n}\hat{\sigma}_n^{\dagger}\hat{\sigma}_n \otimes \left(\sum_{\nu} C_{n,\nu}\hat{R}_{n,\nu}\right), \tag{4}$$

with $C_{n,\nu}$ being the exciton–phonon coupling strength between nth exciton and νth phonon mode.

To compute the non-linear molecular response, the dipole operator is defined as

$$\hat{\mu} = \sum_{n}^{N}\mu_n\left(\hat{\sigma}_n^{\dagger} + \hat{\sigma}_n\right), \tag{5}$$

where μ_n is the transition dipole of the nth exciton.

To obtain a matrix representation of $\hat{H}_{\mathrm{Q}}$ and $\hat{\mu}$, we construct a diabatic basis by dressing the exciton states with photonic Fock states within a double excitation subspace as described in Sec. III A of Paper I (Ref. 37). For a system of N two-level excitons coupled to a single cavity mode, the total number of quantum states within the double excitation subspace is $\mathcal{K} = 2N + 3 + N(N-1)/2$, which scales as $\mathcal{O}(N^2)$.

B. PLDM approach for dynamics propagation

The diabatic Hamiltonian of a system coupled to a bath (nuclear DOF) can be expressed as

$$\begin{aligned}\hat{H} &= \frac{\hat{P}^2}{2M} + V_0(\hat{R}) + \sum_{a}^{\mathcal{K}} V_{aa}(\hat{R})|a\rangle\langle a| + \frac{1}{2}\sum_{b\neq a}^{\mathcal{K}} V_{ab}(\hat{R})|a\rangle\langle b| \\ &= \hat{H}_{\mathrm{b}} + \hat{H}_{\mathrm{Q}},\end{aligned} \tag{6}$$

where $\hat{R}$ and $\hat{P}$ are the position and momenta, respectively, of the bath particles of mass M, and $V_0(\hat{R})$ is the state-independent

part of the Hamiltonian. In the context of this work, for the HTC Hamiltonian,

$$\hat{H}_{\mathrm{b}} = \frac{\hat{P}^2}{2M} + V_0(\hat{R}),$$
$$\hat{H}_{\mathrm{Q}} = \sum_a^{\mathcal{N}} V_{aa}(\hat{R})|a\rangle\langle a| + \frac{1}{2}\sum_{b\neq a}^{\mathcal{N}} V_{ab}(\hat{R})|a\rangle\langle b|,$$

where $\hat{H}_{\mathrm{Q}}$ is the quantum part of the Hamiltonian [see Eq. (2)]. Here, we use $\hat{R}$ as a short-hand notation for $\{\hat{R}_{n,v}\}$.

As described in Paper I,[37] the PLDM approach evolves the reduced density matrix of the system by propagating the forward and backward quantum coefficients (mapping variables) and coupling to the classical equation of motion for the nuclear DOF. Although the original PLDM approach[39–43] was developed based on the partially linearized path-integral formalism using the Meyer–Miller–Stock–Thoss (MMST) mapping representation, it can be recast using forward and backward expansion coefficients c_a and $\tilde{c}_a$ (see discussions in Paper I[37]), evolving according to

$$i\hbar\dot{c}_a(t) = \sum_b V_{ab}(R(t))\cdot c_b(t), \tag{7a}$$

$$-i\hbar\dot{\tilde{c}}_a(t) = \sum_b V_{ab}(R(t))\cdot \tilde{c}_b(t). \tag{7b}$$

The nuclear DOFs evolve according to

$$\frac{\partial R}{\partial t} = P, \quad \frac{\partial P}{\partial t} = \mathcal{F}, \tag{8a}$$

$$\mathcal{F} = -\frac{1}{2}\nabla_R\big(\mathcal{H}(R) + \tilde{\mathcal{H}}(R)\big), \tag{8b}$$

where the MMST mapping Hamiltonian for the forward coefficients is expressed as

$$\mathcal{H} = \frac{P^2}{2M} + V_0(R) + \sum_a V_{aa}(R)|c_a|^2 + \sum_{b\neq a} V_{ab}(R)(\mathfrak{Re}[c_a]\mathfrak{Re}[c_b] + \mathfrak{Im}[c_a]\mathfrak{Im}[c_b]), \tag{9}$$

and a similar expression for $\tilde{\mathcal{H}}$ can be obtained using the backward coefficients,

$$\tilde{\mathcal{H}} = \frac{P^2}{2M} + V_0(R) + \sum_a V_{aa}(R)\cdot|\tilde{c}_a|^2 + \sum_{b\neq a} V_{ab}(R)(\mathfrak{Re}[\tilde{c}_a]\mathfrak{Re}[\tilde{c}_b] + \mathfrak{Im}[\tilde{c}_a]\mathfrak{Im}[\tilde{c}_b]). \tag{10}$$

The reduced density matrix estimator (for each individual trajectory) can be expressed as

$$\hat{\rho}_{\mathrm{Q}} = |\Psi\rangle\langle\tilde{\Psi}|, \tag{11}$$

where the forward and backward vectors are expanded in these coefficients as

$$|\Psi\rangle = \sum_a^{\mathcal{K}} c_a|a\rangle \quad \text{and} \quad \langle\tilde{\Psi}| = \sum_a^{\mathcal{K}} \tilde{c}_a\langle a|. \tag{12}$$

It should be noted that the dynamics for the quantum subsystem are not unitary due to coupling to the bath and $\hat{\rho}_{\mathrm{Q}}$ does not correspond to a pure state, and upon the trajectory average, Eq. (11) describes reduced density matrix for mixed states. The time-dependent reduced density matrix of the system is obtained by averaging $\hat{\rho}_{\mathrm{Q}}$ from all trajectories. For the system with an initial state of $\hat{\rho}_{\mathrm{Q}}(0) = c_{n_0}|n_0\rangle\langle\tilde{n}_0|\tilde{c}_{\tilde{n}_0}$, the elements of the reduced system density matrix can now be obtained as

$$\langle n_j|\hat{\rho}_{\mathrm{Q}}(t)|\tilde{n}_j\rangle = \left(\frac{1}{2}c_{n_j}(t)\cdot c^*_{n_0}\right)\cdot\left(\frac{1}{2}\tilde{c}^*_{\tilde{n}_j}(t)\cdot\tilde{c}_{\tilde{n}_0}\right). \tag{13}$$

C. 2DES spectroscopy

Within the linear response limit, the 2D electronic spectra can be obtained by computing the third order response from the four-point correlation function,[8,44]

$$R^{(3)}(t_1,t_2,t_3) = -i\,\mathrm{Tr}\left[\hat{\mu}(t_3+t_2+t_1)\hat{\mu}^{\times}(t_2+t_1)\hat{\mu}^{\times}(t_1)\hat{\mu}^{\times}(0)\hat{\rho}^{(g)}\right], \tag{14}$$

where $\hat{\mu}^{\times}\hat{A} \equiv [\hat{\mu},\hat{A}]$ and $\hat{\rho}^{(g)}$ is the equilibrium ground state of the system.[37] Here, the system is perturbed at times t_0, t_1, and t_2 and the system response is detected at t_3. In Eq. (14), $R^{(3)}$ can be separated into eight different Liouville pathways, each can be categorized as either rephasing or non-rephasing signals. Four of these Liouville pathways correspond to

$$R_1^{(3)} = -i\,\mathrm{Tr}\left[\hat{\mu}(t_3+t_2+t_1)\hat{\mu}(0)\hat{\rho}_g\hat{\mu}(t_1)\hat{\mu}(t_1+t_2)\right], \tag{15a}$$

$$R_2^{(3)} = -i\,\mathrm{Tr}\left[\hat{\mu}(t_3+t_2+t_1)\hat{\mu}(t_1)\hat{\rho}_g\hat{\mu}(0)\hat{\mu}(t_2+t_1)\right], \tag{15b}$$

$$R_3^{(3)} = -i\,\mathrm{Tr}\left[\hat{\mu}(t_3+t_2+t_1)\hat{\mu}(t_2+t_1)\hat{\rho}_g\hat{\mu}(0)\hat{\mu}(t_1)\right], \tag{15c}$$

$$R_4^{(3)} = -i\,\mathrm{Tr}\left[\hat{\mu}(t_3+t_2+t_1)\hat{\mu}(t_2+t_1)\hat{\mu}(t_1)\hat{\mu}(0)\hat{\rho}_g\right], \tag{15d}$$

while the other four pathways can be constructed from the complex conjugate of Eqs. (15a)–(15d). The purely absorptive 2D spectra is computed by adding the rephasing (denoted as $R^{(3)}_{\mathrm{rep}}$) and non-rephasing (denoted as $R^{(3)}_{\mathrm{nrp}}$) contributions expressed as follows:

$$R^{(3)}_{\mathrm{rep}}(t_1,t_2,t_3) = R_2^{(3)} + R_3^{(3)} + R_1^{(3)*}, \tag{16a}$$

$$R^{(3)}_{\mathrm{nrp}}(t_1,t_2,t_3) = R_1^{(3)} + R_4^{(3)} + R_2^{(3)*}. \tag{16b}$$

In Eqs. (16a) and (16b), the terms on the right-hand side are arranged as individual contributions from (in the order of) stimulated emission (SE), ground state bleach (GSB), and excited state absorption (ESA) signals, respectively. The 2D spectra in the frequency domain are calculated by performing separate Fourier transforms of rephasing and non-rephasing signals,

$$R^{(3)}_{\mathrm{rep}}(\omega_1,t_2,\omega_3) = \int_0^{T_1} dt_1 \int_0^{T_3} dt_3 R^{(3)}_{\mathrm{rep}} e^{i\omega_3 t_3 - i\omega_1 t_1} S_1 S_3, \tag{17a}$$

$$R^{(3)}_{\mathrm{nrp}}(\omega_1,t_2,\omega_3) = \int_0^{T_1} dt_1 \int_0^{T_3} dt_3 R^{(3)}_{\mathrm{nrp}} e^{i\omega_3 t_3 + i\omega_1 t_1} S_1 S_3, \tag{17b}$$

where $S_i = \cos(\pi t_i / 2T_i)$ is the smoothing function for time t_i. The frequency domain pure absorptive 2D spectra is the imaginary part of the total contribution from rephasing [Eq. (17a)] and non-rephasing [Eq. (17b)] signals, expressed as follows:

$$R^{(3)}(\omega_1,t_2,\omega_3) = -\Im\mathrm{m}\left[R^{(3)}_{\mathrm{rep}}(\omega_1,t_2,\omega_3) + R^{(3)}_{\mathrm{nrp}}(\omega_1,t_2,\omega_3)\right]. \tag{18}$$

D. Simulating 2DES using PLDM

The nonlinear responses in Eq. (14) can be equivalently expressed as[44]

$$R^{(3)}(t_1,t_2,t_3) = -i\,\mathrm{Tr}\left[\hat{\mu}\,\mathcal{G}_3\left(\hat{\mu}^{\times}\,\mathcal{G}_2\left(\hat{\mu}^{\times}\,\mathcal{G}_1\left(\hat{\mu}_0^{\times}\hat{\rho}^{(g)}\right)\right)\right)\right], \tag{19}$$

where $\mathcal{G}_j\hat{A} = e^{\frac{i}{\hbar}\hat{H}t_j}\hat{A}e^{-\frac{i}{\hbar}\hat{H}t_j}$. As a specific example, the non-rephasing ground state bleach (GSB) signal in Eq. (15d) can be written as[44]

$$R^{(3)}_4(t_1,t_2,t_3) = -i\,\mathrm{Tr}\Big[\hat{\mu}e^{\frac{i}{\hbar}\hat{H}t_3}\hat{\mu}e^{\frac{i}{\hbar}\hat{H}t_2}\hat{\mu}e^{\frac{i}{\hbar}\hat{H}t_1} \times (\hat{\mu}\hat{\rho}_0)e^{-\frac{i}{\hbar}\hat{H}t_1}e^{-\frac{i}{\hbar}\hat{H}t_2}e^{-\frac{i}{\hbar}\hat{H}t_3}\Big]. \tag{20}$$

These expressions in Eqs. (19) and (20) can be easily evaluated by using the PLDM approximation,[44] where the path-integral expression for the forward and backward propagators are used and the partial linearization approximation on the nuclear DOF is applied.[39,41] For $R^{(3)}$, the PLDM expression is[44]

$$\begin{aligned} R^{(3)}(t_1,t_2,t_3) \approx -i \sum_{n_3}\sum_{n_2,\tilde{n}_2}\int d\tau_2 [\hat{\mu}\tilde{\rho}^{(3)}]_{n_3,n_3} \\ \times \sum_{n_1,\tilde{n}_1}\int d\tau_1 [\hat{\mu}^{\times}\tilde{\rho}^{(2)}]_{n_2,\tilde{n}_2} \\ \times \sum_{n_0,\tilde{n}_0}\int d\tau_0 [\hat{\mu}^{\times}\tilde{\rho}^{(1)}]_{n_1,\tilde{n}_1}[\hat{\mu}\hat{\rho}_g]_{n_0,\tilde{n}_0}\cdot[\hat{\rho}_{\mathrm{b}}]_{\mathrm{w}} \end{aligned} \tag{21}$$

and more specifically for $R^{(3)}_4$, the PLDM expression is

$$\begin{aligned} R^{(3)}_4(t_1,t_2,t_3) \approx -i \sum_{n_3}\sum_{n_2,\tilde{n}_2}\int d\tau_2 [\hat{\mu}\tilde{\rho}^{(3)}]_{n_3,n_3} \\ \times \sum_{n_1,\tilde{n}_1}\int d\tau_1 [\hat{\mu}\tilde{\rho}^{(2)}]_{n_2,\tilde{n}_2}\sum_{n_0,\tilde{n}_0}\int d\tau_0 [\hat{\mu}\tilde{\rho}^{(1)}]_{n_1,\tilde{n}_1} \\ \times [\hat{\mu}\hat{\rho}_g]_{n_0,\tilde{n}_0}\cdot[\hat{\rho}_{\mathrm{b}}]_{\mathrm{w}}. \end{aligned} \tag{22}$$

In the above-mentioned expression, $d\tau_j$ are expressed as

$$d\tau_j \equiv dR_j \cdot dP_j \cdot d\mathbf{c}_j \cdot d\tilde{\mathbf{c}}_j \cdot G_j \cdot \tilde{G}_j, \tag{23}$$

where R_j and P_j are the "initial" nuclear configuration at time t_j, $\mathbf{c}_j \equiv \{c_a(t_j)\}$ and $\tilde{\mathbf{c}}_j \equiv \{\tilde{c}_a(t_j)\}$ are the complex forward and backward coefficients, respectively, at time t_j. Here, the time t_j (for $t_j \in \{t_1,t_2,t_3\}$) are the times at which the system is perturbed with a laser. The quantity $\tilde{\rho}^{(j)}$ represents the reduced system density matrix after applying the perturbation at time t_{j-1}, with an initial state of $\tilde{\rho}^{(j-1)} = c_{n_{j-1}}|n_{j-1}\rangle\langle\tilde{n}_{j-1}|\tilde{c}^*_{\tilde{n}_{j-1}}$ and evolved during the time $t \in [t_{j-1}, t_j]$. The evolved density matrix elements can be expressed as

$$\langle n_j|\tilde{\rho}^{(j)}|\tilde{n}_j\rangle = \left(\frac{1}{2}c_{n_j}(t_j)\cdot c^*_{n_{j-1}}\right)\cdot\left(\frac{1}{2}\tilde{c}^*_{\tilde{n}_j}(t_j)\cdot\tilde{c}_{\tilde{n}_{j-1}}\right). \tag{24}$$

The other response functions have a similar expression as Eq. (22), with $\hat{\mu}$ showing up in different places with $\tilde{\rho}^{(j)}$.

From Eq. (20), one can easily observe that, for each consecutive laser operation, one needs to spawn more trajectories due to the sum, $\sum_{n_j\tilde{n}_j}$, and each $d\tau_j$ contains additional Gaussian sampling for the mapping variables. To reduce this scaling in the number of trajectories, Provazza *et al.*[44] suggested an efficient strategy with focusing and importance sampling techniques[8,41,45] to stochastically choose one pair of labels $\{n_j, \tilde{n}_j\}$, with details outlined in the following section.

E. Focusing scheme of $\hat{\mu}\tilde{\rho}^{(n)}$

The focusing algorithm for the PLDM 2DES simulation requires an stochastic sampling[41,44,45] of the "element" $\{n_j, \tilde{n}_j\}$, based on the weight of the absolute magnitude of the $\hat{\mu}\tilde{\rho}^{(n)}$, and re-weight each trajectory based on the phase of $\hat{\mu}\tilde{\rho}^{(n)}$. This is done by using the importance sampling procedure outlined in the previous work.[8,41,44] The application of a laser at a given time on the system can be represented by the dipole operator acting on the system density matrix estimator. We can expand this as

$$\hat{\mu}\tilde{\rho}^{(n)} = \sum_{ab}[\hat{\mu}\tilde{\rho}^{(n)}]_{ab}|a\rangle\langle b| = \sum_{ab} r_{ab}\cdot e^{i\theta_{ab}}|a\rangle\langle b|, \tag{25}$$

where we decompose the estimator as its absolute value r_{ab} and its phase $e^{i\theta_{ab}}$.

The cumulative distribution function (CDF) is generated from the absolute value of this density matrix,

$$\hat{D} = \sum_{ab} d_{ab}|a\rangle\langle b|, \;\; d_{ab} = \sum_{n\le a}\sum_{m\le b} r_{nm}. \tag{26}$$

Defining the normalization factor (for a total of $\mathcal{K}$ states),

$$\mathcal{R}_\rho = \sum_{a=1}^{\mathcal{K}}\sum_{b=1}^{\mathcal{K}} r_{ab}, \tag{27}$$

we use the normalized CDF for the focusing step.[8] Next, we sample a uniform random number, ζ, and select the collective index $K \equiv ab$, such that

$$\frac{d_{K-1}}{\mathcal{R}_\rho} \le \zeta < \frac{d_K}{\mathcal{R}_\rho}. \tag{28}$$

The pair of the label $\{a,b\}$ will be chosen, and that trajectory will be re-weighted by the phase factor $e^{i\theta_{ab}}$. A diagrammatic illustration of computing $R^{(3)}_1(t_1,t_2,t_3)$ (the SE signal) with the focusing scheme can be found in Fig. 2 of Ref. 8.

The condition in Eq. (28) is typically searched by enumerating all possible $K = \{a,b\}$ and then performing the search over $\mathcal{K}^2$ elements.[8,44] To compute $\hat{\mu}\tilde{\rho}^{(n)}$, in principle, one will need

to multiply two $\mathcal{K}^2$ size matrices. Furthermore, from Eq. (26), in order to calculate the CDF[8,44] of this large matrix, we need to perform another $\mathcal{K}^2$ operation on $\hat{\mu}\tilde{\rho}^{(n)}$. This is a challenging task for computing polariton spectra under the collective coupling regime, with respect to both time and memory requirements as $\mathcal{K} \propto N^2$, especially with a large N.

To reduce the computational cost of the focusing, we modify the original importance sampling algorithm mentioned above as follows. Within a single trajectory, the reduced density matrix of the system can be represented as the outer product of a "forward" ($|\Psi\rangle$) and a "backward" ($\langle\tilde{\Psi}|$) part [see Eq. (11)],

$$\tilde{\rho}^{(n)} = |\Psi\rangle\langle\tilde{\Psi}|. \tag{29}$$

It should be noted that the above-mentioned expression indicates an outer product of pure states for the quantum subsystem associated with a single trajectory. Upon trajectory averaging, the reduced density matrix will describe the mixed states. The operation of the dipole operator on $\tilde{\rho}^{(n)}$ can thus be rewritten as

$$\hat{\mu}\tilde{\rho}^{(n)} = \hat{\mu}|\Psi\rangle\langle\tilde{\Psi}| = (\hat{\mu}|\Psi\rangle)\langle\tilde{\Psi}| = |\Phi\rangle\langle\tilde{\Psi}|, \tag{30}$$

where $|\Phi\rangle = \hat{\mu}|\Psi\rangle$, which can efficiently be evaluated as shown in Eq. (49) of Ref. 37 (paper I), with a linear scaling of the total number of states $\mathcal{K}$. With this, we further express

$$|\Phi\rangle = \sum_a c_a|a\rangle = \sum_a r_a e^{i\theta_a}|a\rangle, \tag{31a}$$

$$\langle\tilde{\Psi}| = \sum_b \tilde{c}_b\langle b| = \sum_b \tilde{r}_b e^{i\theta_b}\langle b|. \tag{31b}$$

Because of this, the density matrix estimator can be expressed as the outer product, and the sum of all elements [in Eq. (27)] can now be simplified as

$$\mathcal{R}_\rho = \sum_{ab} r_{ab} = \left(\sum_a r_a\right)\cdot\left(\sum_b \tilde{r}_b\right) = \mathcal{R}\cdot\tilde{\mathcal{R}}, \tag{32}$$

where $\mathcal{R} = \sum_a r_a$ and $\tilde{\mathcal{R}} = \sum_b \tilde{r}_b$. We also define the cumulative sum of magnitudes as

$$d_a = \sum_{n\le a} r_n, \quad \tilde{d}_b = \sum_{m\le b} \tilde{r}_m. \tag{33}$$

A search for the forward index is equivalent to searching for the row of the focused element. We start the search of the row index a first, with a fixed column index b, for which Eq. (28) is satisfied as

$$\frac{d_{ab}}{\mathcal{R}_\rho} \ge \zeta. \tag{34}$$

Because $d_{ab} = d_a\tilde{d}_b$ and $\tilde{d}_b \le \tilde{R}$ [see Eqs. (32) and (33)], we necessarily have the condition $d_{ab} \le d_a\cdot\tilde{\mathcal{R}}$. Thus, the condition in Eq. (34) becomes

$$\frac{d_{ab}}{\mathcal{R}_\rho} \ge \zeta \Rightarrow \frac{d_a\cdot\tilde{\mathcal{R}}}{\mathcal{R}_\rho} \ge \zeta \Rightarrow \frac{d_a\cdot\tilde{\mathcal{R}}}{\mathcal{R}\cdot\tilde{\mathcal{R}}} \ge \zeta,$$

leading to

$$\frac{d_a}{\mathcal{R}} \ge \zeta, \tag{35a}$$

so the index a is the row of the focused element as long as $d_a/\mathcal{R} \ge \zeta$. Once a row index a is found, one can search the column index b with the following condition:

$$\left(\frac{d_a}{\mathcal{R}}\right)\cdot\tilde{d}_b \ge \zeta, \tag{35b}$$

where ζ and d_a are the same as used in Eq. (35a). The algorithm in Eqs. (35a) and (35b) is equivalent to the original condition in Eq. (28), but significantly reduces the computational cost from order $\mathcal{O}(\mathcal{K}^2)$ to order $\mathcal{O}(2\mathcal{K})$, and there is no need to generate and store the reduced density matrix, $\hat{\mu}\tilde{\rho}^{(n)}$ with $\mathcal{K}^2$ elements.

F. Final response function

To calculate the nth order response, we need to evaluate the following trace within each trajectory:

$$R^{(n)} = \mathrm{Tr}\left[\hat{\mu}\tilde{\rho}^{(n)}\right]. \tag{36}$$

For any forward–backward trajectory methods,[39–43,46,47] we can directly use Eq. (30) to obtain the form

$$R^{(n)} = \mathrm{Tr}\left[|\Phi\rangle\langle\tilde{\Psi}|\right] = \langle\tilde{\Psi}|\Phi\rangle. \tag{37}$$

This is basically the scalar product between the two wavefunctions. Thus, we end up not generating the entire reduced density matrix of order $\mathcal{O}(\mathcal{K}^2)$ to calculate the response using forward–backward methods. Instead, we compute the dot product of the forward and backward wavefunctions with just $\mathcal{K}$ elements.

III. COMPUTATIONAL METHOD

A. Computational scaling with N

For an N-molecule polaritonic system, including the second excitation manifold leads to a $\mathcal{K} \propto \mathcal{O}(N^2)$ number of states, and $\mathcal{O}(N^4)$ numbers of the reduced density matrix elements. The operation of acting $\hat{H}_Q$ on $\hat{\rho}_Q$ would, in principle, require $\mathcal{O}(N^6)$ operations. The total cost of 2DES simulation for the N-molecule polaritonic system, for M trajectories, will be $\mathcal{O}(N^6T^3M)$. This scaling is for both memory and computational cost (run time). However, using the strategies developed in the previous sections, one never needs to generate any $\mathcal{O}(N^4)$ density matrix, and all our calculations can be performed with vectors of the size of $\mathcal{O}(N^2)$. This is the case for any semi-classical or mixed quantum–classical trajectory-based approach, as we extensively discussed in Paper I.[37]

For a time step Δt (where the nuclear configuration is fixed), the propagation of the reduced density matrix can be expressed as applying the unitary propagator $\hat{U}(\Delta t)$

$$\hat{\rho}_Q(\Delta t) = \hat{U}^\dagger(\Delta t)\hat{\rho}_Q\hat{U}(\Delta t) = \hat{U}^\dagger(\Delta t)|\Psi\rangle\langle\tilde{\Psi}|\hat{U}(\Delta t). \tag{38}$$

The forward–backward representation allows us to reduce Eq. (38) operation of order $\mathcal{O}(N^6)$ to the individual operations of $(\hat{U}^\dagger(\Delta t)|\Psi\rangle)$ and $(\langle\tilde{\Psi}|\hat{U}(\Delta t))$, each of which with the cost of

$\mathcal{O}(N^4)$. Furthermore, the matrix–vector and matrix–matrix multiplications reduce to simple Hadamard products as shown in Eq. (27) of Ref. 37 (Paper I), and the usage of Eq. (42) from Paper I to represent the matrix exponential, reduces the cost of density matrix dynamics further, from order $\mathcal{O}(N^4)$ to order $\mathcal{O}(N^2)$.

In Fig. 1, we present the computational scaling cost of different schemes for the operation of Hamiltonian ($\hat{H}_Q$) of the reduced density matrix of the system ($\hat{\rho}_Q$) or the system state vector ($|\Psi\rangle$). The solid red curve is the computational cost of performing a $\hat{H}_Q\hat{\rho}_Q$ operation. Each of the matrices $\hat{H}_Q$ and $\hat{\rho}_Q$ scales as $\mathcal{O}(N^4)$, and thus, their multiplication here scales as $\mathcal{O}(N^6)$, as can be seen in the red curve. The solid yellow curve demonstrates the computational cost of performing a $\hat{H}_Q|\Psi\rangle$ operation, which scales as $\mathcal{O}(N^4)$. The solid cyan curve is the cost of simulating the vectorized sparse $\hat{H}_Q|\Psi\rangle$ operation and scales as $\mathcal{O}(N^2)$. The dotted curves represent the computational time taken by these operations when performed on a GPU.[48–50] Performing the same calculations on the GPU shows a constant scaling, $\mathcal{O}(N^0)$, with increasing N. Although the matrix–vector operation, $\hat{H}_Q\hat{\rho}_Q$, seems very efficient on GPU, these operations occupy a lot of memory, and thus, we are restricted to only a few $\hat{H}_Q\hat{\rho}_Q$ operations. $\hat{H}_Q|\Psi\rangle$ reduces the memory requirement, but we are still highly restricted in the number of $\hat{H}_Q|\Psi\rangle$ operations we can perform. To address this challenge, we move to vectorized $\hat{H}_Q|\Psi\rangle$ operation, where the memory requirement is significantly reduced to a more tractable regime, and we can simultaneously perform a lot of Hadamard products with a reduced computational cost. The improved computational efficiency by GPU is rooted in the working of the GPU architecture itself. The conventional way for CPUs to perform matrix multiplications $\hat{H}_Q|\Psi\rangle$ is to loop over the three indices and operate over each element one at a time, thus giving matrix–matrix multiplication a computational complexity of $\mathcal{O}(\mathcal{K}^3)$, which leads to time scaling of $\mathcal{O}(\mathcal{K}^3)$ if the operations are performed serially. For GPUs, if the memory size of the GPU is larger than the memory storage needed for the matrices, the loops are not needed and all operations are performed together in parallel. Thus, the computation time (and not the complexity itself) reduces to $\mathcal{O}(1)$.

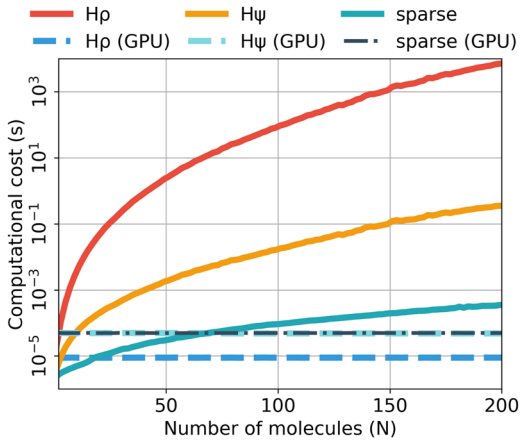

FIG. 1. Computational cost of different matrix multiplications as a function of number of molecules. The red, yellow, and cyan solid curves represent the $\hat{H}_Q\hat{\rho}_Q$, $\hat{H}_Q|\Psi\rangle$, and sparse $\hat{H}_Q|\Psi\rangle$ operations, respectively, performed on CPU. These computations were performed on Intel Xeon E5-2680 v3 @ 2.50 GHz CPU. The dotted lines represent the corresponding GPU calculations that were performed on NVIDIA Hopper H100 GPU.[48] The dark blue lines represent $\hat{H}_Q\hat{\rho}_Q$, the light cyan represents $\hat{H}_Q|\Psi\rangle$, and the dark gray represents the vectorized $\hat{H}_Q|\Psi\rangle$.

B. Vectorization over lasers and trajectories

Since each of the trajectories is independent in the PLDM[39,44] or $\mathcal{L}$-PLDM[8,37] approach, the simulation can be trivially parallelized[51] over a total of M trajectories. This drastically reduces the cost of the computation from an order of $\mathcal{O}(N^2)\mathcal{O}(T^3)\mathcal{O}(M)$ to an order $\mathcal{O}(N^2)\mathcal{O}(T^3)$. Now, we can further make use of the simplified Hadamard products [Eq. (28) of Paper I, Ref. 37] to vectorize the code over each of the laser perturbations, which can, in principle, remove the scaling with respect to T, and thus, our computation can, in principle, be further reduced.

The vectorization[48,52,53] is achieved by grouping multiple trajectories through the collection of the state vector from "m" different trajectories as different columns of a "batch" matrix, $\{|\Psi\rangle\}_m$, of size $\mathcal{K} \times m$,

$$\{|\Psi\rangle\}_m \to \begin{bmatrix} \vdots & \vdots & & \vdots & \vdots \\ |\Psi_1\rangle & |\Psi_2\rangle & \cdots & |\Psi_{(m-1)}\rangle & |\Psi_m\rangle \\ \vdots & \vdots & & \vdots & \vdots \end{bmatrix}, \tag{39}$$

where $|\Psi_i\rangle$ is the key at a certain nuclear time step for the ith trajectory, and similarly, for the propagation of backward coefficients, we can make a batch matrix $\{\langle\Psi|\}_m$ by collecting $\langle\Psi_i|$ from "m" different trajectories. Similarly, we can also bunch together the diagonal energy fluctuations from these trajectories as columns of a batch matrix $\{\epsilon\}_m$, of size $\mathcal{K} \times m$,

$$\{\epsilon\}_m = \begin{bmatrix} \vdots & \vdots & & \vdots & \vdots \\ \epsilon_1 & \epsilon_2 & \cdots & \epsilon_{(m-1)} & \epsilon_m \\ \vdots & \vdots & & \vdots & \vdots \end{bmatrix}, \tag{40}$$

where ϵ_i is the vector containing diagonal fluctuation of site energies for the ith trajectory,

$$\epsilon_i \to \begin{bmatrix} \varepsilon_1 + \sum_\nu C_{1,\nu}R_{1,\nu} \\ \varepsilon_2 + \sum_\nu C_{2,\nu}R_{2,\nu} \\ \vdots \\ \varepsilon_N + \sum_\nu C_{N,\nu}R_{N,\nu} \end{bmatrix}. \tag{41}$$

Here, $C_{n,\nu}$ is the coupling of nth exciton to the νth bath mode coordinate ($R_{n,\nu}$) within the ith trajectory. Using Eqs. (39) and (40), we can convert the simple Hadamard product in Eq. (28) of Paper I (Ref. 37) as a collective Hadamard product of "m" trajectories through the Hadamard product between the batch matrices, $\{\epsilon\}_m \odot \{|\Psi\rangle\}_m$.

Similarly, we can also collectively bunch the position coordinates of bath DOF's (R) from "m" different trajectories,

$$\{R\}_m = \begin{bmatrix} \vdots & \vdots & & \vdots & \vdots \\ R_1 & R_2 & \cdots & R_{(m-1)} & R_m \\ \vdots & \vdots & & \vdots & \vdots \end{bmatrix}, \tag{42}$$

where R_i represents the vector containing position coordinates of all excitons for the ith trajectory (not to be confused with the nuclear

DOF $R_{n,v}$, as we used a shorthand notation for $R = \{R_{n,v}\}$). Similarly, we can collect the momentum coordinates from the "m" trajectories to construct the batch matrix, $\{P\}_m$. These $\{R\}_m$ and $\{P\}_m$ can be collectively propagated using the simple forms of Eqs. (8a) and (8b).

Applying a laser perturbation at different nuclear time steps leads to different initial conditions for each time step. Each of these initial conditions can now be treated as equivalent to a different trajectory as each of these initial conditions will evolve independently of the other. Within each trajectory, we can thus group together all the quantum states after the application of laser perturbation at a certain time step as different columns of the batch matrix, $\{|\Psi\rangle\}^{(i)}$, for the ith trajectory, to construct a matrix of size $\mathcal{K} \times T$,

$$\{|\Psi\rangle\}^{(i)} = \begin{bmatrix} \vdots & \vdots & & \vdots \\ \hat{\mu}|\Psi_i(t_1)\rangle & \hat{\mu}|\Psi_i(t_2)\rangle & \cdots & \hat{\mu}|\Psi_i(t_T)\rangle \\ \vdots & \vdots & & \vdots \end{bmatrix}, \tag{43}$$

where $\hat{\mu}|\Psi_i(t)\rangle$ can be evaluated using Eqs. (35a) and (35b), and $\{|\Psi\rangle\}^{(i)}$ can be propagated just like $\{|\Psi\rangle\}_m$ in Eq. (39). We can also bunch together "m" with different $\{|\Psi\rangle\}^{(i)}$ to make a bigger batch matrix of size $(\mathcal{K} \times T) \times m$,

$$\{\Psi\}_m = \begin{bmatrix} \{|\Psi\rangle\}^{(1)} & \{|\Psi\rangle\}^{(2)} & \cdots & \{|\Psi\rangle\}^{(m)} \end{bmatrix}. \tag{44}$$

Figure 2 presents the computational cost of 2DES simulation at various levels of vectorization for different laser pulses as a function of the number of time steps for a single laser pulse. The red curve is the computational cost for a simple 2DES calculation using the most straightforward coding without any vectorization. If we vectorize the propagations for the time steps between any two laser pulses, we reduce the computational cost from $\mathcal{O}(T^3)$ to $\mathcal{O}(T^2)$, as can be seen from the yellow curve. Vectorization over two propagation periods further reduces the cost to a linear scaling, $\mathcal{O}(T)$, represented by the green curve. If we vectorize over all three propagation segments, we get a constant scaling $\mathcal{O}(T^0)$. It should be noted that, although very efficient, the vectorization over time costs a lot of memory and to actually get a constant scaling, one needs to have a reasonably large GPU resource per trajectory. To get the most out of the available resources, one may need to compromise on the levels of vectorization we do. However, with the above-mentioned scheme, we have a way to systematically control the level of vectorization and parallelization, if the level of computational resource is no longer the limiting factor.

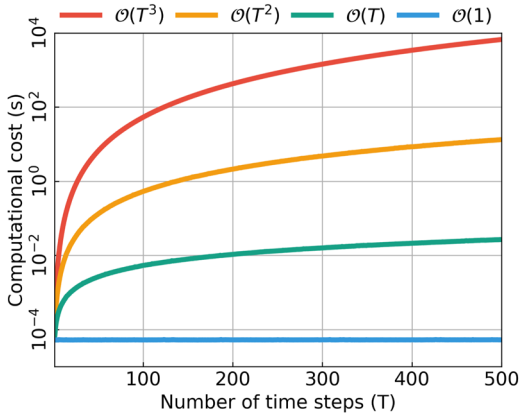

FIG. 2. Computational cost scaling as a function of the number of time steps (T) of each laser pulse delay at different levels of vectorization of Eq. (39). The red curve denotes the computational cost of serial computation for a single trajectory of three laser pulses. The yellow curve denotes the computational cost when one of the lasers is vectorized. The green curve is the case of vectorization along two laser pulses and the blue curve denotes vectorization along all the laser delays. Each curve involves propagating a wavefunction in the 2D excitation manifold of ≈50 molecules with around 2500 total quantum states. The above-mentioned calculations were performed on NVIDIA Hopper H100 GPUs using pytorch[48–50] with device "meta." Each of the curves above is averaged over 10^6 instances of Eq. (39) operations.

C. Computational details

The phonon frequencies and coupling strength are sampled from the Debye spectral density,[54]

$$J_m(\omega) = \frac{\pi}{2}\sum_v \frac{C_{m,v}^2}{\omega_{m,v}}\delta(\omega - \omega_{m,v}) = \frac{2\lambda_b\omega_0\omega}{\omega_0^2 + \omega^2}, \tag{45}$$

with λ_b being the bath reorganization energy and ω_0 being the characteristic frequency of the bath. For all the calculations, we sampled 20 bath modes for each of the exciton sites.

The 2DES calculations were performed by including the second excitation subspace. To restrict the total size of Hilbert space, we simulate the 2DES for $N = 1$ (with $\mathcal{K} = 5$), $N = 2$ (with $\mathcal{K} = 8$), $N = 5$ (with $\mathcal{K} = 23$), and $N = 25$ (with $\mathcal{K} = 228$) molecules coupled to the single cavity mode. We choose the average site energy of the molecules to be $\langle\varepsilon\rangle = \sum_n \varepsilon_n/N = 0.5$ eV, and the cavity mode is tuned to molecular excitation energy, $\hbar\omega_c = 0.5$ eV (see the discussions in Appendix A from Ref. 37 for the choice of parameters, and the logic of the shift in $\langle\varepsilon\rangle$). The total Rabi splitting was fixed at $\Omega_c = 2\sqrt{N}\hbar g_c = 0.1$ eV. For Figs. 3–5, we do not consider any cavity

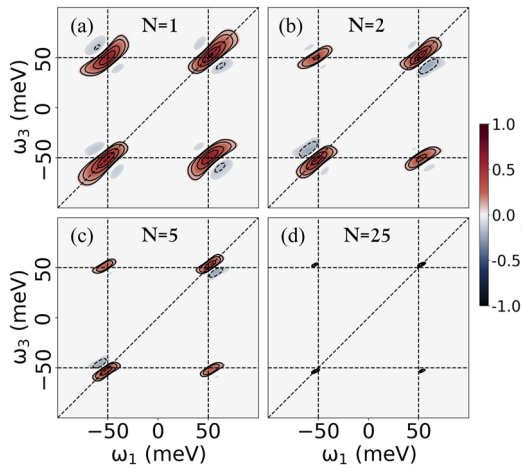

FIG. 3. Rephasing 2D spectra for polaritonic systems containing various numbers of molecules. Panels (a)–(d) represent the rephasing spectra of $N = 1, 2, 5$, and 25, respectively.

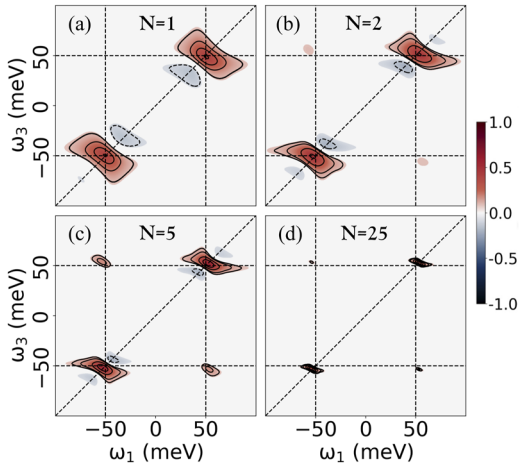

FIG. 4. Non-rephasing 2D spectra for polaritonic systems containing various numbers of molecules. Panels (a)–(d) represent the nonrephasing spectra of $N = 1$, 2, 5, and 25, respectively.

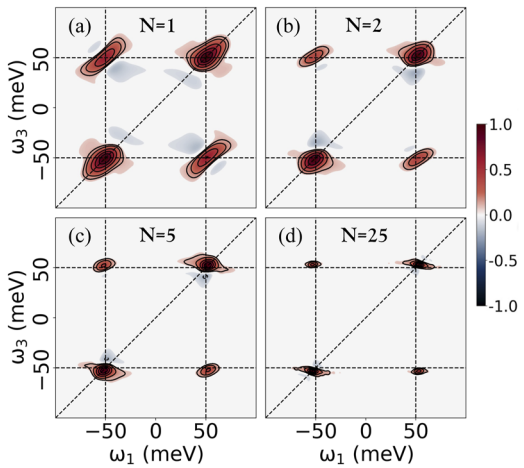

FIG. 5. Pure absorptive spectra for polaritonic systems containing various numbers of molecules. Panels (a)–(d) show the total pure-absorptive spectra $N = 1, 2, 5$, and 25, respectively.

loss, and we only simulate the 2DES at $t_2 = 0$ fs to clearly demonstrate the changes in lineshape, purely due to collective effects. We set the nuclear time step to be 40 au (≈1 fs). Since the coherence lifetime increases with increasing N, we need longer T_1 and T_3. For $N = 1$ and $N = 2$, we set $T_1 = T_3 = 400$ fs. For $N = 5$, we use $T_1 = T_3 = 500$ fs, and for $N = 25$, we use $T_1 = T_3 = 1000$ fs.

For Figs. 7 and 8, we consider the cavity loss rate $\Gamma_c = 10$ meV using the stochastic $\mathcal{L}$-PLDM algorithm.[8,37,55] Here, we used a nuclear time step of 20 au (≈0.5 fs) and $T_1 = T_3 = 300$ fs.

IV. RESULTS AND DISCUSSIONS

Figures 3(a)–3(d) shows the rephasing signal for $N = 1, 2, 5$, and 25, respectively. In panel (a), we observe four diagonally elongated peaks with one molecule coupled to the cavity mode. The lower diagonal peak at ($\hbar\omega_1 \approx -50$ meV, $\hbar\omega_3 \approx -50$ meV) corresponds to the lower polariton excitation, and the upper diagonal peak at ($\hbar\omega_1 \approx 50$ meV, $\hbar\omega_3 \approx 50$ meV) corresponds to the upper polariton excitation. The cross peaks at ($\hbar\omega_1 \approx -50$ meV, $\hbar\omega_3 \approx 50$ meV) and at ($\hbar\omega_1 \approx 50$ meV, $\hbar\omega_3 \approx -50$ meV) correspond to coherent energy transfer between the upper and lower polaritonic states. In panel (b), we present the rephasing 2DES for two molecules coupled to the cavity mode. All the peaks are diagonally elongated and appear at a location similar to that in panel (a). With increasing N, we can observe a significant reduction in the linewidth of various peaks due to the polaron decoupling effect[30,31,37,56–58] (that the reorganization energy $\lambda \propto 1/N$), even though $\sqrt{N}\hbar g_c$ is fixed. This linewidth narrowing with an increasing N is also evident in the linear spectra.[30,37] The size of all the peaks is reduced, which is equivalent to the reduction of polariton linewidths in the linear spectra with increasing N, as shown in Figs. 4 and 5 of Paper I.[37] In addition, we also see the appearance of an asymmetrical negative signal (derivative lineshape) in both the lower and upper diagonal peaks. This is observed because of the excited-state absorption transitions (ESA) from the upper and lower polaritons to higher double exciton states in the double excitation manifold,[9,59,60] which is only possible for $N > 1$. As such, the appearance of this ESA peak is a signature of the collective coupling of molecules to the cavity mode. As we increase the number of molecules to $N = 5$ in panel (c), the peaks appear at locations similar to those in panels (a) and (b), but the size is further reduced. There are dark states for $N = 2$, $N = 5$, and $N = 25$. Due to their zero net transition dipole, they are not visible in 2DES presented in panels (b)–(d)

Figures 4(a)–4(d) present the non-rephasing response signal intensity for different N. Panel (a) presents the non-rephasing signal for one molecule coupled to the cavity. The peaks along the diagonals appear at the same location as the diagonal peaks in Fig. 3 but are aligned along the anti-diagonal direction and they correspond to the lower and upper polariton locations. Panels (b)–(d) represent the non-rephasing signals for $N = 2$, 5, and 25 molecules coupled to the cavity, respectively. The peak size decreases with an increasing number of molecules because of the linewidth reduction as we observed in linear spectra in Fig. 4 of Paper I.[37] The off-diagonal coherence peaks also appear in the same locations as the rephasing signals but they become relatively more intense with an increasing number of molecules.[31] It should be noted that in Figs. 3 and 4, we have individually normalized the intensity for each panel relative to the maximum intensity. The off-diagonal coherence peak is indeed larger in the non-rephasing signal compared to the rephasing signal, which is more apparent in the totally absorptive single in Fig. 6, where the off-diagonal shape is dominated by the non-rephasing 2D lineshape. This relative increase in the intensity for the non-rephasing signal compared to the rephasing signal can be attributed to the polaron decoupling effect,[1,30,56,57] which effectively reduces the strength of coupling between polariton states and phonon bath modes. This reduction in system–bath coupling results in an effective decrease in the bath reorganization energy, which decreases the relative contribution from slow bath modes in the spectral density

[low-frequency modes have a larger coupling strength to exciton in the current $J(\omega)$ model than the high-frequency tail of the bath]. The light–matter coupling and the resulting polaron decoupling effect thus decrease the inhomogeneity of the phonon bath environment for the polariton states and hence intensify the relative coherence transfer through non-rephasing pathways. Similar enhancement of polariton coherence has been observed in recent exact quantum dynamics simulations and analytic theory.[31]

Figures 5(a)–5(d) present the total pure-absorptive 2DES for different N, which is obtained by direct addition of the rephasing (Fig. 3) and non-rephasing signals (Fig. 4) and then normalizing the signal according to the maximum peak intensity. Panel (a) presents the pure-absorptive 2DES of one molecule coupled to the cavity mode. The upper and lower diagonal peaks correspond to the upper and lower polariton eigenstates. These peaks are overall diagonally elongated, indicating that the polaritonic states are coupled to an inhomogenous bath environment. Panel (b) represents the pure absorptive 2DES of $N = 2$ molecules coupled to the cavity. The overall size of the peaks has reduced, and the diagonal peaks appear to have relatively reduced in the diagonal direction (the homogeneous broadening has become very similar to the inhomogeneous broadening). We also see the appearance of ESA signatures in the diagonal peaks, which is due to the formation of double-exciton states that allow for the transitions between single excitons in the first excitation manifold with the double excitons in the second excitation manifold. Comparing all the panels, we can observe that with an increase in N, the overall linewidth becomes homogenous and the 2DES is mostly dominated by the non-rephasing pathways. This is due to the effective reduction of coupling strength between the polariton states and the bath modes, which makes the non-rephasing pathways more favorable, as discussed above.

Figure 6 presents different Liouville pathways for the different signals used in pure-absorptive 2DES. The vertical direction represents the increasing time of propagation. The light-red and sky-blue arrows represent the system perturbation with the external laser field. The light-red arrow pointing in the right direction represents an electric field with a negative phase factor ($e^{-i\omega t}$, where ω is the frequency of the radiation field), and the sky-blue arrow, pointing in the left direction represents the electric field with a positive phase factor ($e^{i\omega t}$). The vertical yellow, dark-red, and dark-blue arrows represent the evolution of the system after the first, second, and third laser perturbations, respectively. Within the ladders, we represent the state of the system as either coherence or population states. For example, $|G_0\rangle$ corresponds to the collective ground state, $|P_1\rangle$ ($|P_1'\rangle$ and $|P_1''\rangle$) represent the polariton eigenstates in the first excitation manifold (like the upper polariton, $|+\rangle$ and the lower polariton $|-\rangle$), and $|P_2\rangle$ correspond to the polariton eigenstates in the second excitation manifold.[8,9,37,59,60] Each of the diagrams is read from bottom to up in the vertical direction of increasing time. The detailed definitions of these states are expressed in Eqs. (23) and (24) in Paper I.[37] Different coherence and population transfer mechanisms are further demonstrated in Appendix for the rephasing SE signal.

Figure 7 presents the individual contributions of the rephasing spectra (with GSB, SE, and ESA) for $N = 5$ molecules coupled to the cavity mode as a function of population time t_2. The four columns represent the ground state bleaching (GSB), the simulated emission (SE), the excited state absorption (ESA), and the total rephasing signal, respectively. The three rows

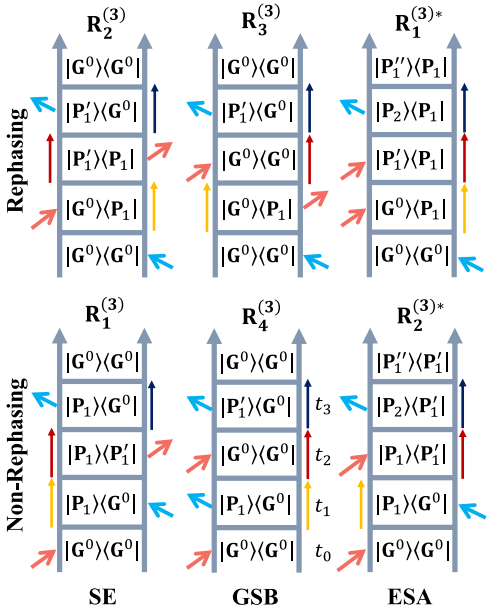

FIG. 6. Liouville pathways for different signal components contributing to the purely absorptive 2D spectra. The vertical direction represents the increasing time axis. The yellow, dark-red, and dark-blue arrows indicate the propagation of the system during t_1, t_2, and t_3 periods, respectively. The light-red arrow pointing to the right indicates the electric field perturbation with a negative phase ($e^{-i\omega t}$), and the sky-blue arrow pointing to the left represents the electric field with a positive phase ($e^{i\omega t}$).

represent the intensities for each of the signals at $t_2 = 0$, 125, and 250 fs, respectively. All signals are individually normalized according to their maximum signal intensity. Panels (a)-(d) represent the GSB, SE, ESA, and total rephasing, respectively, at $t_2 = 0$ fs. In panel (a), we observe diagonally elongated peaks at ($\hbar\omega_1 \approx -50$ meV, $\hbar\omega_3 \approx -50$ meV) and at ($\hbar\omega_1 \approx 50$ meV, $\hbar\omega_3 \approx 50$ meV), which correspond to the energetic locations of the lower and upper polariton eigenstates, respectively. We also observe cross peaks at ($\hbar\omega_1 \approx -50$ meV, $\hbar\omega_3 \approx 50$ meV) and ($\hbar\omega_1 \approx 50$ meV, $\hbar\omega_3 \approx -50$ meV), which indicate the coherent energy transfer between the bright-polariton states.

In Fig. 7(b), we observe very similar lineshapes for the diagonal and cross peaks, as shown in panel (a). This can be interpreted from the Feynman diagrams for these two pathways ($R_2^{(3)}$ and $R_3^{(3)}$ in Fig. 6) at initial population time $t_2 = 0$ fs. For both cases, SE and GSB, during t_1, the system is in the coherence state $|G^0\rangle\langle\pm|$ and during t_3, the system is in the conjugate coherence state $|\pm\rangle\langle G^0|$. Thus, they have exactly the same lineshapes at $t_2 = 0$ fs for all the peaks.

Figure 7(c), we observe the negative ESA peaks to be a little bit shifted from along ω_3, when compared to the peak locations in panels (a) and (b). This is because the $|G^0\rangle \rightarrow |P_1\rangle$ transitions are at slightly different frequencies compared to the $|P_1\rangle \rightarrow |P_2\rangle$ transitions. The overall addition of signals gives the diagonally elongated diagonal and cross peaks in the total rephasing spectra in panel (d). We can observe the existence of negative features along the diagonal peaks due to the shifted contribution from the ESA signal. As

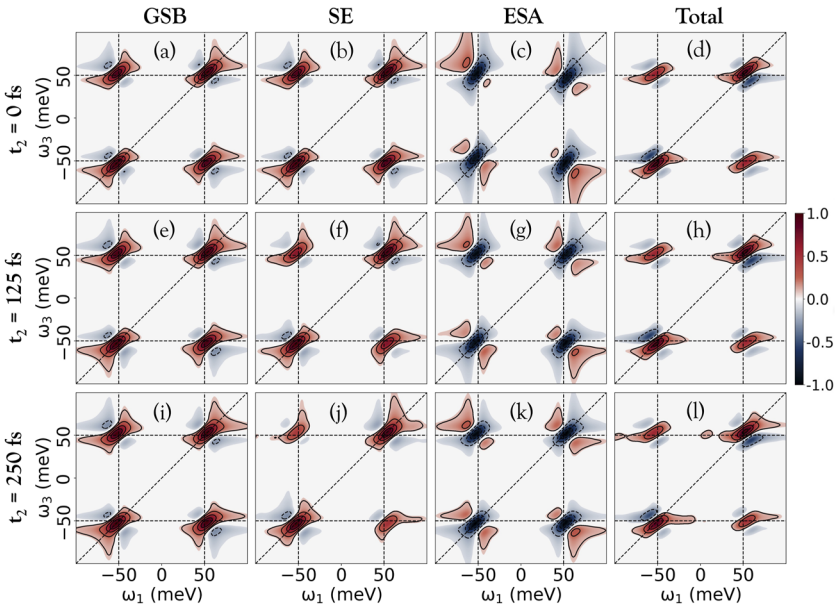

FIG. 7. Rephasing signal for $N = 5$ decomposed for individual contributions including GSB, SE, and ESA for the first three columns, respectively. The last column shows the total rephasing signal. The rows indicate the signal intensities at $t_2 = 0$, 125, and 250 fs, respectively. Panels (a), (e), and (i) show the GSB contributions to the rephasing signal at $t_2 = 0$, 125, and 250 fs, respectively. Panels (b), (f), and (j) show the SE contributions to the rephasing signal at $t_2 = 0$, 125, and 250 fs, respectively. Panels (c), (g), and (k) show the ESA contributions to the rephasing signal at $t_2 = 0$, 125, and 250 fs, respectively. Panels (d), (h), and (l) show the total rephasing signal at $t_2 = 0$, 125, and 250 fs, respectively.

we move down along each column, we see similar lineshape features when compared to the first row. On careful observation, we see that the SE transition cross peak intensities have reduced when compared to the GSB transitions at $t_2 = 250$ fs [see Figs. 7(a) and 7(i) compared to Figs. 7(b) and 7(j)]. This is due to the population decay associated with the cavity mode during population time t_2. For the SE signal, the system is in the state $|\pm\rangle\langle\pm|$ (see Fig. 9), which loses its intensity when evolving during t_2 due to cavity loss from the cavity mode ($|G^1\rangle \rightarrow |G^0\rangle$). When the cross peak intensity of the SE signal is compared to the GSB signal cross peak at $t_2 = 250$ fs, where the system is in the state $|G^0\rangle\langle G^0|$ during t_2 propagation, which increases in intensity due to the decay of photonic population to the ground state. The effect of difference in population between the $|\pm\rangle\langle\pm|$ and $|G^0\rangle\langle G^0|$ during t_2 causes the cross peaks to be significantly reduced in size for the SE signal, and thus the GSB pathway is the major contributor to the coherent energy transfer between the polariton eigenstates via the rephasing mechanism.

In Fig. 8, we present the similar decomposition of the non-rephasing spectra at different population times, t_2, for $N = 5$ molecules coupled to the cavity mode. Panels (a)-(d) represent the

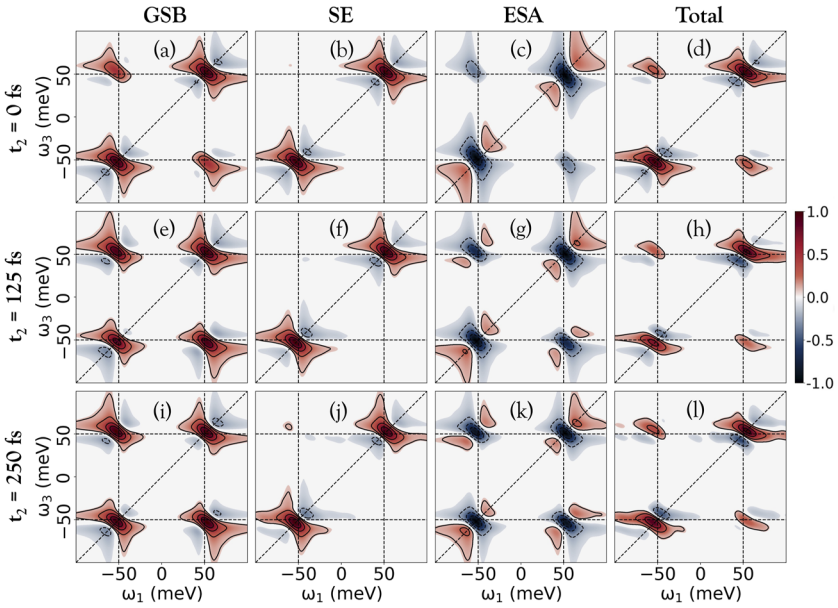

FIG. 8. Non-rephasing signal for $N = 5$ decomposed for individual contributions, including GSB, SE, and ESA for the first three columns, respectively. The last column shows the total non-rephasing signal. The rows indicate the signal intensities at $t_2 = 0$, 125, and 250 fs, respectively. Panels (a), (e), and (i) show the GSB contributions to the non-rephasing signal at $t_2 = 0$, 125, and 250 fs, respectively. Panels (b), (f), and (j) show the SE contributions to the non-rephasing signal at $t_2 = 0$, 125, and 250 fs, respectively. Panels (c), (g), and (k) show the ESA contributions to the non-rephasing signal at $t_2 = 0$, 125, and 250 fs, respectively. Panels (d), (h), and (l) show the total non-rephasing signal at $t_2 = 0$, 125, and 250 fs, respectively.

GSB, SE, ESA, and the total non-rephasing spectra at $t_2 = 0$ fs. In panel (a), we observe the appearance of anti-diagonally elongated peaks at ($\hbar\omega_1 \approx -50$ meV, $\hbar\omega_3 \approx -50$ meV) and ($\hbar\omega_1 \approx 50$ meV, $\hbar\omega_3 \approx 50$ meV), which are the location of lower and upper polariton eigenstates, respectively. We also observe the cross peaks at ($\hbar\omega_1 \approx -50$ meV, $\hbar\omega_3 \approx 50$ meV) and ($\hbar\omega_1 \approx 50$ meV, $\hbar\omega_3 \approx -50$ meV), indicating the coherent energy transfer between the bright-polariton eigenstates via the non-rephasing GSB pathway. Due to its non-rephasing nature, the cross peaks are also anti-diagonally elongated. As we move to panel (b), we see the appearance of SE peaks only along the diagonals, but no cross peaks. Upon inspecting the Feynman diagram corresponding to the non-rephasing SE signal ($R_1^{(3)}$), coherent energy transfer through this pathway is not possible. If during t_1, the system is in the coherence state $|+\rangle\langle G^0|$ (or $|-\rangle\langle G^0|$), then following the SE pathway, it will end up again in the coherence state $|+\rangle\langle G^0|$ (or $|-\rangle\langle G^0|$) during t_3 and so we do not observe any cross peaks. In panel (c), we present the ESA spectrum with the appearance of diagonal peaks, which are relatively shifted along the ω_3 axis when compared to the diagonal peaks of SE and GSB. Just like the rephasing ESA pathway, this can again be attributed to the difference of transition energies when exciting from first to second excited manifold in comparison with ground to first excited manifold. Panel (d) represents the overall non-rephasing spectra at $t_2 = 0$ fs. The diagonal peaks appear at the same location as in GSB and SE signals. The cross peaks appear at the same location as the cross peaks of the total rephasing spectra and the overall intensity is mostly dominated by the contribution from GSB and SE signals. As we move down in each column, the relative lineshapes remain comparable to early t_2 but the contribution from the ESA signal is increasing in the overall non-rephasing signal as can be verified by the increase in the negative ESA signal along the diagonal peaks in panels (d), (h), and (l).

V. CONCLUSION

In this paper, we extended the $\mathcal{L}$-PLDM formalism to simulate the non-linear spectra for N-molecules collectively coupled to the cavity, described by the HTC Hamiltonian. A direct density-matrix-based simulation will require a computational cost (in both time and memory requirements) proportional to $\mathcal{O}(N^6)$. The sparse nature of the HTC system Hamiltonian and dipole matrix lets us compactly express $\hat{H}_Q|\Psi_s\rangle$ and $\hat{\mu}|\Psi_s\rangle$ as simple Hadamard products between vectors of $\mathcal{O}(N^2)$ instead of matrix–matrix or matrix–vector operations. We further utilize the forward–backward nature of the $\mathcal{L}$-PLDM method to convert all matrix–matrix operations to consecutive vector–vector Hadamard products. Here, we incorporated these strategies into the previously developed $\mathcal{L}$-PLDM approach for simulating 2D electronic spectra (2DES) of exciton–polariton under the collective coupling regime. In particular, we apply the efficient quantum dynamics propagation scheme developed in Paper I[37] to both the forward and the backward propagations in the $\mathcal{L}$-PLDM approach[8,37,55] and develop an efficient importance sampling scheme and GPU vectorization scheme that allows us to systematically reduce the computational costs from $\mathcal{O}(\mathcal{K}^2)\mathcal{O}(T^3)$ to $\mathcal{O}(\mathcal{K})\mathcal{O}(T^0)$ for the 2DES simulation, where $\mathcal{K}$ is the number of states and T is the number of time steps of propagation.

We have simulated the 2DES of up to $N = 25$ molecules coupled to the cavity within the double excitation subspace and demonstrated the reduction in 2D lineshapes of both the diagonal and cross peaks. These spectroscopic features have been observed experimentally in Ref. 1, where the coupling of molecules to the cavity mode leads to a reduction in the 2D linewidth of the lower polariton diagonal peak. The same feature is also observed in Refs. 6 and 7, where the coupling of molecular J-aggregates to a plasmonic mode reduces the 2D lineshapes of polariton diagonal and cross peaks.

We further analyzed the signal from both rephasing and non-rephasing contributions, as well as the ground state bleaching (GSB), excited state emission (ESA), and stimulated emission (SE). For $N > 1$, we also found the derivative lineshape due to ESA, which appears as a negative feature on the lower and upper polariton diagonal peaks due to the difference in frequencies of $|G\rangle \rightarrow |P_1\rangle$ and $|P_1\rangle \rightarrow |P_2\rangle$ transitions.[9,59,60] This is similar to the observations made by DelPo *et al.* in Ref. 9.

Together with Paper I,[37] the theoretical developments that we presented here allow an efficient and accurate simulation of quantum dynamics[37,61,62] and multi-dimensional spectroscopy of exciton polariton under the collective coupling regimes, which we envision will benefit the future investigations of molecular polaritons.

ACKNOWLEDGMENTS

This work was supported by the Department of Energy under Grant No. DE-SC0022171 as well as by the National Science Foundation Award under Grant No. CHE-2244683. M.E.M. acknowledges the support from the Wu Fellowship by the Department of Chemistry at the University of Rochester. P.H. acknowledges the support from his Cottrell Scholar Award (a program by the Research Corporation for Science Advancement). Computing resources were provided by the Center for Integrated Research Computing (CIRC) at the University of Rochester. M.E.M. thanks Ben Chng for valuable discussions and comments. P.H. thanks Minjung Son for valuable discussions of polariton 2DES. We also thank Professor David Jonas for his pioneer work on Femtosecond multidimensional spectroscopy, which inspired this work.

AUTHOR DECLARATIONS

Conflict of Interest

The authors have no conflicts to disclose.

Author Contributions

M. Elious Mondal: Conceptualization (lead); Data curation (lead); Formal analysis (lead); Investigation (lead); Methodology (lead); Software (lead); Validation (lead); Visualization (lead); Writing – original draft (lead); Writing – review & editing (equal). **A. Nickolas Vamivakas**: Conceptualization (equal); Funding acquisition (equal); Investigation (supporting); Project administration (equal); Writing – original draft (supporting); Writing – review & editing (supporting). **Steven T. Cundiff**: Conceptualization (equal); Formal analysis (equal); Funding acquisition (equal); Project administration (equal); Supervision (equal); Writing – original draft

(supporting); Writing – review & editing (supporting). **Todd D. Krauss**: Conceptualization (equal); Formal analysis (equal); Funding acquisition (lead); Investigation (equal); Project administration (equal); Supervision (equal); Writing – original draft (supporting); Writing – review & editing (supporting). **Pengfei Huo**: Conceptualization (lead); Formal analysis (equal); Funding acquisition (equal); Investigation (equal); Methodology (equal); Project administration (lead); Resources (equal); Supervision (lead); Validation (equal); Visualization (equal); Writing – original draft (equal); Writing – review & editing (lead).

DATA AVAILABILITY

The data that support the findings of this work are available from the corresponding author on a reasonable request.

APPENDIX: LIOVILLE PATHWAYS FOR THE REPHASING SIMULATED EMISSION SIGNAL

All the different Liouville pathways shown in Fig. 6 can be further broken down into several subpathways depending on which eigenstates (excluding bath Hamiltonian) the system is transitioning during the laser perturbation, and how excitation energy is being transitioned to other states due to bath fluctuations. Here, we present a simple overview of the possible pathways leading to the different peak locations for the rephasing SE signal.

In Fig. 9, we present different energy transfer pathways after different laser perturbations. For example, if we follow the left-most pathway, the initial system is in the ground state $|G^0\rangle\langle G^0|$ and being perturbed from "right" by the laser causing the system to transition to the coherence state $|G^0\rangle\langle+|$. The system then propagates in this state for a time t_1, oscillating at a frequency ω_+ with a phase $e^{i\omega_+ t_1}$, which is then perturbed from "left," causing the system to transition to the population state $|+\rangle\langle+|$. The system decays in this state for time t_2 due to the loss of the photon mode, after which it is perturbed by the third laser from the right, stimulating the system to cause emission back to the ground state. The system is now in coherence between the upper polariton and the ground state, $|+\rangle\langle G^0|$, which oscillates at a frequency of ω_+ for t_3 with a phase factor of $e^{-i\omega_+ t_3}$, after which the system emits a signal giving a SE signal at the location ($\hbar\omega_1 \approx 50$ meV, $\hbar\omega_3 \approx 50$ meV). We see that the system oscillates with opposite phases during t_1 and t_3, giving it the rephasing nature.

If we follow the second pathway, the second perturbation takes the system to a coherence between lower and upper polariton $|-\rangle\langle+|$ and so the system state evolves with a frequency of $\omega_- - \omega_+$ for time t_2. After the third perturbation, the system transitions to a coherence between lower polariton and ground state, $|-\rangle\langle G^0|$. Thus, during t_3, the system propagates with a phase of $e^{-i\omega_- t_3}$. Due to two different frequency oscillations during t_1 and t_3, we get a cross peak at ($\hbar\omega_1 \approx 50$ meV, $\hbar\omega_3 \approx -50$ meV). In addition, since during the population time, t_2, the system is in the coherence state $|-\rangle\langle+|$ propagating with a phase factor $e^{-i(\omega_- - \omega_+)t_2}$, as we scan the 2DES with t_2, we observe the cross peak intensity oscillating at a frequency of the Rabi splitting ($\hbar\Omega_R = \hbar\omega_+ - \hbar\omega_-$).

In a similar way, we can also analyze the third pathway, which mirrors the second pathway, in that we swap the lower and upper polaritons to obtain an upper cross peak at ($\hbar\omega_1 \approx -50$ meV, $\hbar\omega_3 \approx 50$ meV). In addition, since in this pathway, during the population time, t_2, the system state ($|+\rangle\langle-|$) is oscillating with Rabi frequency (with a phase $e^{-i(\omega_+ - \omega_-)t_2}$), this cross-peak oscillates with the Rabi frequency with t_2.

Finally, the fourth pathway can be obtained by replacing the upper polaritons ($|+\rangle$ and $\langle+|$) with the lower polaritons ($|-\rangle$ and $\langle-|$) in the first pathway, which produces the lower diagonal peak ($\hbar\omega_1 \approx -50$ meV, $\hbar\omega_1 \approx -50$ meV). During the population time (t_2), the system state ($|-\rangle\langle-|$) decays due to the photonic loss without any oscillations and so the lower diagonal peak intensity will only decay with time without any oscillations (unlike the cross peaks).

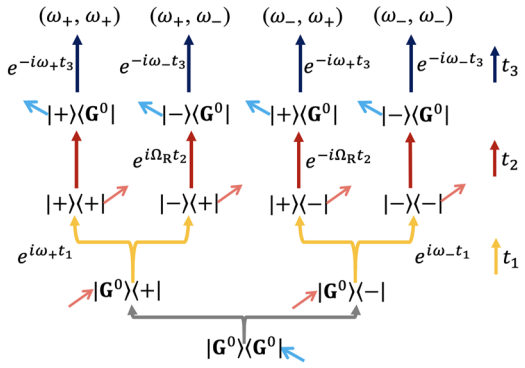

FIG. 9. Liouville pathway for rephasing SE with different polaritonic bright states. The arrow conventions are the same as in Fig. 6 with the yellow, dark-red, and dark-blue arrows indicating the system propagation after the first, second, and third laser perturbations for t_1, t_2, and t_3 intervals, respectively. The sky-blue arrow pointing to the left indicates that the phase of the electric field is positive ($e^{i\omega t}$) and the light-red arrows pointing to the right indicate that the phase of the electric field is negative ($e^{-i\omega t}$). The last row indicates the peak location in the 2D spectra due to the specific pathway, followed where ω_+ and ω_- are the energetic location of upper and lower polariton eigenstates, respectively.

REFERENCES

[1] S. Takahashi and K. Watanabe, "Decoupling from a thermal bath via molecular polariton formation," J. Phys. Chem. Lett. **11**, 1349–1356 (2020).
[2] T. M. Autry, G. Nardin, C. L. Smallwood, K. Silverman, D. Bajoni, A. Lemaître, S. Bouchoule, J. Bloch, and S. Cundiff, "Excitation ladder of cavity polaritons," Phys. Rev. Lett. **125**, 067403 (2020).
[3] M. Son, Z. T. Armstrong, R. T. Allen, A. Dhavamani, M. S. Arnold, and M. T. Zanni, "Energy cascades in donor-acceptor exciton-polaritons observed by ultrafast two-dimensional white-light spectroscopy," Nat. Commun. **13**, 7305 (2022).
[4] N. Peruffo, F. Mancin, and E. Collini, "Coherent dynamics in solutions of colloidal plexcitonic nanohybrids at room temperature," Adv. Opt. Mater. **11**, 2203010 (2023).
[5] L. Mewes, M. Wang, R. A. Ingle, K. Börjesson, and M. Chergui, "Energy relaxation pathways between light-matter states revealed by coherent two-dimensional spectroscopy," Commun. Phys. **3**, 157 (2020).
[6] T. Quenzel, D. Timmer, M. Gittinger, J. Zablocki, F. Zheng, M. Schiek, A. Lützen, T. Frauenheim, S. Tretiak, M. Silies *et al.*, "Plasmon-enhanced exciton delocalization in squaraine-type molecular aggregates," ACS Nano **16**, 4693–4704 (2022).
[7] D. Timmer, M. Gittinger, T. Quenzel, S. Stephan, Y. Zhang, M. F. Schumacher, A. Lützen, M. Silies, S. Tretiak, J.-H. Zhong *et al.*, "Plasmon mediated coherent population oscillations in molecular aggregates," Nat. Commun. **14**, 8035 (2023).

[8]M. E. Mondal, E. R. Koessler, J. Provazza, A. N. Vamivakas, S. T. Cundiff, T. D. Krauss, and P. Huo, "Quantum dynamics simulations of the 2D spectroscopy for exciton polaritons," J. Chem. Phys. **159**, 094102 (2023).
[9]C. A. DelPo, B. Kudisch, K. H. Park, S.-U.-Z. Khan, F. Fassioli, D. Fausti, B. P. Rand, and G. D. Scholes, "Polariton transitions in femtosecond transient absorption studies of ultrastrong light–molecule coupling," J. Phys. Chem. Lett. **11**, 2667–2674 (2020).
[10]T. Virgili, D. Coles, A. Adawi, C. Clark, P. Michetti, S. Rajendran, D. Brida, D. Polli, G. Cerullo, and D. Lidzey, "Ultrafast polariton relaxation dynamics in an organic semiconductor microcavity," Phys. Rev. B **83**, 245309 (2011).
[11]S. Renken, R. Pandya, K. Georgiou, R. Jayaprakash, L. Gai, Z. Shen, D. G. Lidzey, A. Rao, and A. J. Musser, "Untargeted effects in organic exciton–polariton transient spectroscopy: A cautionary tale," J. Chem. Phys. **155**, 154701 (2021).
[12]B. Liu, V. M. Menon, and M. Y. Sfeir, "Ultrafast thermal modification of strong coupling in an organic microcavity," APL Photonics **6**, 016103 (2021).
[13]D. M. Jonas, "Two-dimensional femtosecond spectroscopy," Annu. Rev. Phys. Chem. **54**, 425–463 (2003).
[14]J. D. Hybl, A. W. Albrecht, S. M. Gallagher Faeder, and D. M. Jonas, "Two-dimensional electronic spectroscopy," Chem. Phys. Lett. **297**, 307–313 (1998).
[15]J. D. Hybl, A. Albrecht Ferro, and D. M. Jonas, "Two-dimensional Fourier transform electronic spectroscopy," J. Chem. Phys. **115**, 6606–6622 (2001).
[16]S. M. Gallagher Faeder and D. M. Jonas, "Two-dimensional electronic correlation and relaxation spectra: Theory and model calculations," J. Phys. Chem. A **103**, 10489–10505 (1999).
[17]M. Cho, H. M. Vaswani, T. Brixner, J. Stenger, and G. R. Fleming, "Exciton analysis in 2D electronic spectroscopy," J. Phys. Chem. B **109**, 10542 (2005).
[18]T. Brixner, J. Stenger, H. M. Vaswani, M. Cho, R. E. Blankenship, and G. R. Fleming, "Two-dimensional spectroscopy of electronic couplings in photosynthesis," Nature **434**, 625–628 (2005).
[19]S. Biswas, J. Kim, X. Zhang, and G. D. Scholes, "Coherent two-dimensional and broadband electronic spectroscopies," Chem. Rev. **122**, 4257–4321 (2022).
[20]G. D. Scholes, G. R. Fleming, L. X. Chen, A. Aspuru-Guzik, A. Buchleitner, D. F. Coker, G. S. Engel, R. Van Grondelle, A. Ishizaki, D. M. Jonas *et al.*, "Using coherence to enhance function in chemical and biophysical systems," Nature **543**, 647–656 (2017).
[21]P. Hamm and M. Zanni, *Concepts and Methods of 2D Infrared Spectroscopy* (Cambridge University Press, 2011).
[22]E. Fresch, F. V. Camargo, Q. Shen, C. C. Bellora, T. Pullerits, G. S. Engel, G. Cerullo, and E. Collini, "Two-dimensional electronic spectroscopy," Nat. Rev. Methods Primers **3**, 84 (2023).
[23]S. Mukamel, *Principles of Nonlinear Optical Spectroscopy* (Oxford University Press on Demand, 1999), Vol. 6.
[24]L. Valkunas, D. Abramavicius, and T. Mancal, *Molecular Excitation Dynamics and Relaxation: Quantum Theory and Spectroscopy* (John Wiley & Sons, 2013).
[25]A. M. Brańczyk, D. B. Turner, and G. D. Scholes, "Crossing disciplines—A view on two-dimensional optical spectroscopy," Ann. Phys. **526**, 31–49 (2014).
[26]A. Gelzinis, R. Augulis, V. Butkus, B. Robert, and L. Valkunas, "Two-dimensional spectroscopy for non-specialists," Biochim. Biophys. Acta, Bioenerg. **1860**, 271–285 (2019).
[27]E. Collini, "2D electronic spectroscopic techniques for quantum technology applications," J. Phys. Chem. C **125**, 13096–13108 (2021).
[28]E. O. Odewale, S. T. Wanasinghe, and A. S. Rury, "Assessing the determinants of cavity polariton relaxation using angle-resolved photoluminescence excitation spectroscopy," J. Phys. Chem. Lett. **15**, 5705–5713 (2024).
[29]E. O. Odewale, A. G. Avramenko, and A. S. Rury, "Deciphering between enhanced light emission and absorption in multi-mode porphyrin cavity polariton samples," Nanophotonics **13**, 2695–2706 (2024).
[30]W. Ying, M. E. Mondal, and P. Huo, "Theory and quantum dynamics simulations of exciton-polariton motional narrowing," J. Chem. Phys. **161**, 064105 (2024).
[31]B. X. Chng, W. Ying, Y. Lai, A. N. Vamivakas, S. T. Cundiff, T. D. Krauss, and P. Huo, "Mechanism of molecular polariton decoherence in the collective light–matter couplings regime," J. Phys. Chem. Lett. **15**, 11773–11783 (2024).
[32]M. Du, L. A. Martínez-Martínez, R. F. Ribeiro, Z. Hu, V. M. Menon, and J. Yuen-Zhou, "Theory for polariton-assisted remote energy transfer," Chem. Sci. **9**, 6659–6669 (2018).
[33]G. Sandik, J. Feist, F. J. García-Vidal, and T. Schwartz, "Cavity-enhanced energy transport in molecular systems," Nat. Mater. (published online 2024).
[34]Z. Zhang, X. Nie, D. Lei, and S. Mukamel, "Multidimensional coherent spectroscopy of molecular polaritons: Langevin approach," Phys. Rev. Lett. **130**, 103001 (2023).
[35]D. Gallego-Valencia, L. Mewes, J. Feist, and J. L. Sanz-Vicario, "Coherent multidimensional spectroscopy in polariton systems," Phys. Rev. A **109**, 063704 (2024).
[36]R. F. Ribeiro, A. D. Dunkelberger, B. Xiang, W. Xiong, B. S. Simpkins, J. C. Owrutsky, and J. Yuen-Zhou, "Theory for nonlinear spectroscopy of vibrational polaritons," J. Phys. Chem. Lett. **9**, 3766–3771 (2018).
[37]M. E. Mondal, A. N. Vamivakas, S. T. Cundiff, T. D. Krauss, and P. Huo, "Polariton spectra under the collective coupling regime. I. Efficient simulation of linear spectra and quantum dynamics," J. Chem. Phys. **162**, 014114 (2025).
[38]A. Mandal, M. A. Taylor, B. M. Weight, E. R. Koessler, X. Li, and P. Huo, "Theoretical advances in polariton chemistry and molecular cavity quantum electrodynamics," Chem. Rev. **123**, 9786–9879 (2023).
[39]P. Huo and D. F. Coker, "Communication: Partial linearized density matrix dynamics for dissipative, non-adiabatic quantum evolution," J. Chem. Phys. **135**, 201101 (2011).
[40]P. Huo and D. F. Coker, "Semi-classical path integral non-adiabatic dynamics: A partial linearized classical mapping Hamiltonian approach," Mol. Phys. **110**, 1035–1052 (2012).
[41]P. Huo and D. F. Coker, "Consistent schemes for non-adiabatic dynamics derived from partial linearized density matrix propagation," J. Chem. Phys. **137**, 22A535 (2012).
[42]P. Huo, T. F. Miller, and D. F. Coker, "Communication: Predictive partial linearized path integral simulation of condensed phase electron transfer dynamics," J. Chem. Phys. **139**, 151103 (2013).
[43]M. Lee, P. Huo, and D. Coker, "Semiclassical path integral dynamics: Photosynthetic energy transfer with realistic environment interactions," Annu. Rev. Phys. Chem. **67**, 639 (2016).
[44]J. Provazza, F. Segatta, M. Garavelli, and D. F. Coker, "Semiclassical path integral calculation of nonlinear optical spectroscopy," J. Chem. Theory Comput. **14**, 856–866 (2018).
[45]E. Dunkel, S. Bonella, and D. Coker, "Iterative linearized approach to nonadiabatic dynamics," J. Chem. Phys. **129**, 114106 (2008).
[46]J. R. Mannouch and J. O. Richardson, "A partially linearized spin-mapping approach for nonadiabatic dynamics. I. Derivation of the theory," J. Chem. Phys. **153**, 194109 (2020).
[47]J. R. Mannouch and J. O. Richardson, "A partially linearized spin-mapping approach for nonadiabatic dynamics. II. Analysis and comparison with related approaches," J. Chem. Phys. **153**, 194110 (2020).
[48]J. Nickolls, I. Buck, M. Garland, and K. Skadron, "Scalable parallel programming with CUDA: Is CUDA the parallel programming model that application developers have been waiting for?," Queue **6**, 40–53 (2008).
[49]R. Okuta, Y. Unno, D. Nishino, S. Hido, and C. Loomis, "CuPy: A NumPy-compatible library for NVIDIA GPU calculations," in Proceedings of the Workshop on Machine Learning Systems (LearningSys) in The Thirty-First Annual Conference on Neural Information Processing Systems (NIPS), 2017.
[50]A. Paszke, S. Gross, F. Massa, A. Lerer, J. Bradbury, G. Chanan, T. Killeen, Z. Lin, N. Gimelshein, L. Antiga, A. Desmaison, A. Köpf, E. Yang, Z. DeVito, M. Raison, A. Tejani, S. Chilamkurthy, B. Steiner, L. Fang, J. Bai, and S. Chintala, "PyTorch: An imperative style, high-performance deep learning library," in *Proceedings of the 33rd International Conference on Neural Information Processing Systems* (Curran Associates, Inc., Red Hook, NY, 2019).
[51]L. Dalcín, R. Paz, and M. Storti, "MPI for Python," J. Parallel Distrib. Comput. **65**, 1108–1115 (2005).
[52]C. R. Harris, K. J. Millman, S. J. van der Walt, R. Gommers, P. Virtanen, D. Cournapeau, E. Wieser, J. Taylor, S. Berg, N. J. Smith, R. Kern, M. Picus, S. Hoyer, M. H. van Kerkwijk, M. Brett, A. Haldane, J. F. del Río, M. Wiebe, P. Peterson,

P. Gérard-Marchant, K. Sheppard, T. Reddy, W. Weckesser, H. Abbasi, C. Gohlke, and T. E. Oliphant, "Array programming with NumPy," Nature **585**, 357–362 (2020).
[53]S. K. Lam, A. Pitrou, and S. Seibert, "Numba: A LLVM-based python JIT compiler," in *Proceedings of the Second Workshop on the LLVM Compiler Infrastructure in HPC, LLVM '15* (Association for Computing Machinery, New York, 2015).
[54]P. L. Walters, T. C. Allen, and N. Makri, "Direct determination of discrete harmonic bath parameters from molecular dynamics simulations," J. Comput. Chem. **38**, 110–115 (2017).
[55]E. R. Koessler, A. Mandal, and P. Huo, "Incorporating Lindblad decay dynamics into mixed quantum-classical simulations," J. Chem. Phys. **157**, 064101 (2022).
[56]F. Herrera and F. C. Spano, "Cavity-controlled chemistry in molecular ensembles," Phys. Rev. Lett. **116**, 238301 (2016).
[57]F. Herrera and F. C. Spano, "Theory of nanoscale organic cavities: The essential role of vibration-photon dressed states," ACS Photonics **5**, 65–79 (2018).
[58]Y. Lai, W. Ying, and P. Huo, "Non-equilibrium rate theory for polariton relaxation dynamics," J. Chem. Phys. **161**, 104109 (2024).
[59]J. A. Campos-Gonzalez-Angulo, R. F. Ribeiro, and J. Yuen-Zhou, "Generalization of the Tavis–Cummings model for multi-level anharmonic systems," New J. Phys. **23**, 063081 (2021).
[60]J. A. Campos-Gonzalez-Angulo and J. Yuen-Zhou, "Generalization of the Tavis–Cummings model for multi-level anharmonic systems: Insights on the second excitation manifold," J. Chem. Phys. **156**, 194308 (2022).
[61]B. X. K. Chng, M. E. Mondal, W. Ying, and P. Huo, "Quantum dynamics simulations of exciton polariton transport," Nano Lett. **25**, 1617–1622 (2025).
[62]D. Hu, B. Chng, W. Ying, and P. Huo, "Trajectory-based non-adiabatic simulations of the polariton relaxation dynamics," chemRxiv:10.26434/chemrxiv–2024–t818f (2024).